

RESEARCH LETTER

10.1002/2015GL067329

Key Points:

- Our global *S* wave model is evolutionary and will be updated with new data on a regular basis
- We observe no ocean/continent difference in the depth extent of azimuthal anisotropy
- Alignment of olivine crystals is preferentially horizontal and azimuthally random under continents

Supporting Information:

- Supporting Information S1

Correspondence to:

E. Debayle,
Eric.Debayle@ens-lyon.fr

Citation:

Debayle, E., F. Dubuffet, and S. Durand (2016), An automatically updated *S*-wave model of the upper mantle and the depth extent of azimuthal anisotropy, *Geophys. Res. Lett.*, *43*, 674–682, doi:10.1002/2015GL067329.

Received 9 DEC 2015

Accepted 31 DEC 2015

Accepted article online 5 JAN 2016

Published online 30 JAN 2016

An automatically updated *S*-wave model of the upper mantle and the depth extent of azimuthal anisotropy

Eric Debayle¹, Fabien Dubuffet¹, and Stéphanie Durand¹

¹Laboratoire de Géologie de Lyon : Terre, Planètes, Environnement, CNRS, UMR 5276, École Normale Supérieure de Lyon, Université de Lyon, Université Claude Bernard Lyon 1, Villeurbanne, France

Abstract We present 3D2015_07Sv, an *S* wave model of the upper mantle based on the waveform modeling of 1,359,470 Rayleigh waves recorded since 1976. The use of approximate forward theory and modeling allows updating the model with new data on a regular basis. 3D2015_07Sv contains azimuthal anisotropy, achieves a lateral resolution of ~600 km, and is consistent with other recent models up to degree 60 in the uppermost 200 km and degree 15 in the transition zone. Although radial anisotropy has been found to extend deeper beneath continents than beneath oceans, we find no such difference for azimuthal anisotropy, suggesting that beneath most continents, the alignment of olivine crystal is preferentially horizontal and azimuthally random at large scale. As most continents are located on slow moving plates, this supports the idea that azimuthal anisotropy aligns at large scale with the present plate motion only for plates faster than ~4 cm yr⁻¹.

1. Introduction

In the last 20 years, the resolution of global *S* wave upper mantle tomographic models has drastically improved. This is largely due to the increase of available data and to the development of automated approaches able to process hundreds of thousands of surface wave seismograms [e.g., *Trampert and Woodhouse, 1995; van Heijst and Woodhouse, 1997; Debayle, 1999; Beucler et al., 2003; Lebedev and van der Hilst, 2008; Yoshizawa and Ekstrom, 2010; Debayle and Ricard, 2012; Schaeffer and Lebedev, 2013; French et al., 2013*]. The development, over the same period, of more sophisticated theories that account for diffraction or mode coupling [*Spetzler and Snieder, 2001; Marquering et al., 1996; Zhou et al., 2004*] has also offered new possibilities to improve resolution. The most promising approach for surface waves is probably full waveform inversion [*Komatitsch et al., 2002; Tromp et al., 2005; Fichtner et al., 2009, 2010*] which involves the computation of exact synthetic seismograms in a 3-D model and an inversion using the adjoint method. Until now, this approach has only been applied on a regional scale [*Fichtner et al., 2009, 2010; Zhu et al., 2012; Zhu and Tromp, 2013; Chen et al., 2015*], and most recent global *S* wave upper mantle models are built using ray theory [e.g., *Debayle and Ricard, 2012; Schaeffer and Lebedev, 2013*]. An exception is the SEMUM2 model by *French et al.* [2013] which uses a “hybrid” approach, involving the exact computation of 3-D synthetics and an inversion with 2-D sensitivity kernels [*Li and Romanowicz, 1995*].

We use the term “resolution” in a broad sense, defined as the quantity of information that can be extracted from noisy data (the maximum number of independent elastic parameters or the minimum distance across which heterogeneities can be mapped). A variety of approaches exist for resolution analysis [e.g., *Fichtner and van Leeuwen, 2015*]. The “nominal resolution” is mathematically defined in linear inverse theory and derived from a resolution matrix [e.g., *Backus and Gilbert, 1968*]. In this paper, we estimate the nominal resolution from synthetic tests, and we consider that two models are consistent when their correlation is above the 95% confidence level. Synthetic tests suggest that most recent global Sv wave upper mantle models can recover structures ≤800 km [*Debayle and Ricard, 2012; French et al., 2013; Schaeffer and Lebedev, 2013*]. However, comparisons of the different models published show that they are generally consistent up to degree 20–30 (wavelengths ≥1300 km) in the upper 200 km [*Debayle and Ricard, 2012; Meschede and Romanowicz, 2015*]. In the transition zone, the agreement is poorer and confined to harmonic degree ≤10 (wavelength ≥4000 km). There is therefore a gap between the nominal resolution which is estimated through synthetic tests and the size of seismic heterogeneities which is robustly determined and consistent between different seismic

models. This difference is likely due to the fact that the nominal resolution relies in most cases only on data coverage and regularization, while other observational and theoretical effects (period range of analysis, number of overtones considered, data noise, theory used, parameterization, and regularization) also contribute to the observed differences between seismic models.

In this paper, we show that by incorporating more data into seismic models, we can improve their consistency up to the nominal resolution. We also address the question of the depth extent of azimuthal anisotropy beneath continents and oceans. We have built a new Sv wave model, 3D2015_07Sv, based on 1,359,470 Rayleigh waveforms. We requested all vertical component Rayleigh waves associated with events having a centroid moment tensor (CMT) solution (i.e., with $M_w \geq \sim 4.3$), and recorded at permanent stations between 1976 and July 2015, or at stations deployed temporarily in the field in Europe, Africa, Asia, Australia, and French Polynesia. 3D2015_07Sv is the basis of an evolutionary model that will be regularly updated with new data.

2. Building 3D2015_07Sv

2.1. Data

We requested records from IRIS and RESIF data centers starting from the CMT catalog issued at the Lamont-Doherty Earth Observatory of Columbia University. We consider only events listed in the CMT catalog, as we use the CMT solution to compute the source excitation. Those events have a moment magnitude $M_w \geq \sim 4.3$. We requested all Rayleigh waveforms recorded on the LHZ channel by the virtual networks GSN_broadband, FDSN_all, and US_backbone between January 1976 and July 2015. We also used data from Program for Array Seismic Studies of the Continental Lithosphere (PASSCAL) experiments in Africa, Tibet, and New Zealand, from the SKIPPY temporary deployment in Australia and from French temporary experiments in the Horn of Africa [Montagner *et al.*, 2007], French Polynesia [Barruol *et al.*, 2002], and in the Aegean-Anatolia region [Salauen *et al.*, 2012]. About 9.4 million Rayleigh waveforms were obtained from IRIS DMC and REseau Sismologique & géodésique Français (RESIF) data centers.

2.2. Automated Waveform Inversion

Waveforms are analyzed using the automated scheme of Debayle and Ricard [2012]. We summarize here the main steps of the scheme and refer to Debayle and Ricard [2012] for a more detailed description.

A preprocessing stage allows us to select and prepare data for the waveform inversion. We first check for each record that all the necessary information (instrument response and CMT solution) is available. Then, the signal-to-noise ratio is measured at different periods in order to determine the period range of analysis. A signal-to-noise ratio greater than 3 is required over a sufficiently broad period range; otherwise, the data are rejected. This criterion, which is often not fulfilled by small magnitude earthquakes, is responsible for most rejections. During this step, 42% of the initial 9.4 million Rayleigh waveforms are accepted.

About 3.9 million Rayleigh waveforms enter into the automated waveform inversion step. Each waveform is fitted using a synthetic seismogram made by a fundamental mode and a few overtones. Synthetics are computed in a 1-D model adapted to each ray, which includes a path-specific crust structure estimated from the three Dimensional Seismological Model A Priori Constrained (3SMAC) of Nataf and Ricard [1995] and a radially anisotropic upper mantle very close to the Preliminary Reference Earth Model (PREM) [Dziewonski *et al.*, 1981] at a reference period of 100 s. We also invert for a 1-D profile of attenuation. A detailed description of our treatment of the crust and attenuation can be found in Debayle and Ricard [2012]. About 33% of the records pass successfully all stages of the waveform inversion, corresponding to 1,359,470 accepted waveforms. For each waveform, we extract a set of secondary observables for the fundamental mode and up to the fifth overtone. Table S1 in the supporting information summarizes the number of secondary observables as a function of period and mode number. In addition, the waveform inversion yields a path average 1-D shear velocity model compatible with the recorded waveform. Among the successful waveforms, 1,197,740 were modeled in the period range 40–200 s, using synthetic seismograms made by the fundamental mode and up to the fifth overtone, following Debayle and Ricard [2012]. The remaining 161,730 waveforms were recorded for large events ($6.0 < M_w < 7.2$) which excite Rayleigh waves at periods greater than 200 s. These waveforms were modeled by Durand *et al.* [2015], who applied Debayle and Ricard [2012]'s scheme in the period range 100–400 s for the fundamental and up to the second overtone. Durand *et al.* [2015] demonstrated that this longer period data set provides additional information on the shear velocity structure in the depth range 100–1000 km.

The whole data set expands upon *Debayle and Ricard* [2012] and *Durand et al.* [2015] data sets by a factor of 3.5 and 2.5, respectively. To our knowledge, this is the largest surface wave data set assembled today, including 30,469 events and 1630 stations. It includes all the Rayleigh waves that we were able to model at permanent stations between 1976 and 2015, completed by data recorded in several temporary experiments that help to improve global coverage. Figure S1 summarizes the stations and events coverage.

2.3. Tomographic Inversion

The 1,359,470 path average shear velocity models are then combined in a tomographic inversion to produce the “background” 3-D shear velocity model, 3D2015_07Sv.

To decrease the computing time and memory requirement, we cluster at each depth the path-average shear velocity models associated with close epicenters recorded at a given station. Details on the clustering can be found in *Debayle and Ricard* [2012]. After clustering, the 1,359,470 shear velocity models reduces to $\sim 250,000$ clusters corresponding to “independent,” well-resolved path average shear velocities in the uppermost 200 km of the mantle. At larger depths, only intermediate-to-deep events located in subduction zones provide well excited higher modes and well-resolved shear velocities. The number of independent paths decreases to $\sim 100,000$ at 550 km depth, $\sim 40,000$ at 750 km depth, and $\sim 11,000$ at 900 km depth. Compared to DR2012, our previous seismic model [*Debayle and Ricard*, 2012], the number of independent paths is expanded by a factor ~ 2 in the uppermost 200 km and by a factor ~ 5 in the deeper parts of the upper mantle. In addition, 3D2015_07Sv provides constraints in the top of the lower mantle, which was not resolved in DR2012. The number of rays crossing a 600×600 km surface area is displayed at different depths in Figure 1.

The tomographic inversion is performed using the scheme of *Debayle and Sambridge* [2004]. We invert for the local distribution of shear velocity and azimuthal anisotropy. The smoothness of the model is controlled by Gaussian correlation functions which determine the coupling between two locations through an horizontal correlation length L . We use the same values of L for isotropic and anisotropic heterogeneities. L is set to 200 km down to 750 km depth, which means that the model is smoothed over wavelengths of $\sim 3L = 600$ km (distance between two points on each side of the maximum, with amplitude approximately one third of the maximum).

At greater depths, L increases to account for the reduction in the number of paths and reaches 800 km (i.e., smoothing over wavelengths of $\sim 3L = 2400$ km) at 1000 km depth. The strength of heterogeneities is controlled by an a priori model standard deviation of 0.05 km/s for the shear wave velocity. Our experience [*Debayle and Ricard*, 2012] in agreement with previous studies [e.g., *Nishimura and Forsyth*, 1989] shows that this value allows variations of up to $\pm 10\%$ with respect to a 1-D a priori and starting model which is obtained at each depth from the mean of the path average measurements. This a priori and starting model has no azimuthal anisotropy. However, azimuthal variations are allowed in the inverted model, through an a priori standard deviation of 0.005 km/s for the azimuthal anisotropy. This value allows up to $\pm 8\%$ peak to peak azimuthal anisotropy variations in the inverted model. A detailed description of our modeling of azimuthal anisotropy is given in *Debayle and Ricard* [2013]. As we invert for azimuthal anisotropy, the isotropic part of our model is corrected from its effect. This effect is however moderate and does not alter significantly the isotropic part. Increasing L leads to smoother tomographic images, but the overall pattern of anomalies remains unchanged. For comparison with models expressed in spherical harmonics, our model uses spherical harmonics up to the degree $l \sim (2\pi R)/3L \sim 66$, where R is Earth's radius.

2.4. Updating the Model

We update our seismic model following the publication of the monthly CMT catalog. Each update involves enlarging the data set before rerunning the tomographic inversion starting from a 1-D model. For this purpose, we add a layer of automation to the *Debayle and Ricard* [2012]'s waveform modeling scheme. This layer of automation checks from the CMT catalog what are the potential new data available at the GSN_broadband, FDSN_all, and US_backbone virtual networks, requests these data at IRIS DMC using web services, applies the processing chain described in section 2.2 to the new data, and recomputes the seismic model using the procedure defined in section 2.3. A simple shell command launches the model update in an entirely automated way. We found that updating the model with 2 months of data takes about 30 h using 192 cores and allows incorporating $\sim 15,000$ new waveforms into the model.

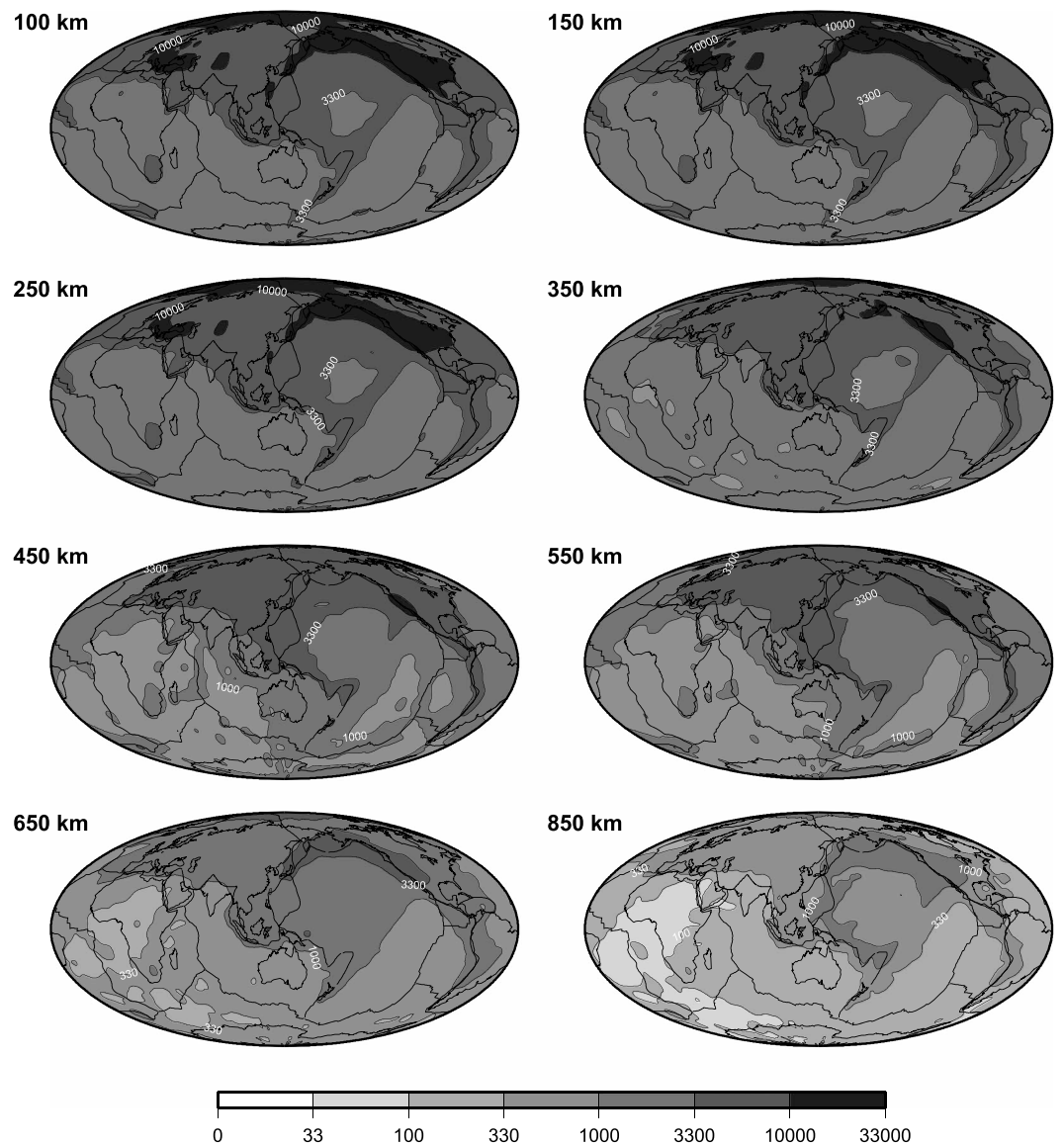


Figure 1. Ray density maps at different depths. Black and white scale indicates the number of rays normalized over a 6 by 6° area.

3. Synthetic Tests and Nominal Resolution

3D2015_07Sv achieves a better horizontal resolution than DR2012. This is due to a denser ray coverage and the use of a smaller horizontal correlation length in the inversion. In order to evaluate the horizontal nominal resolution of 3D2015_07Sv, we performed several synthetic tests that are displayed in Figures S2 and S3. They have been performed using the same a priori choices as in the real inversion.

From these synthetic tests, we estimate the nominal resolution of our model to about 600 km in the uppermost 200 km. At greater depths, although we can still isolate two anomalies distant by 600 km in most regions of the world (Figure S3), the checkerboard test demonstrates that more complex structures with alternating fast and slow velocities are not retrieved in regions with the weakest data sampling (Figure S2).

4. Large-Scale Isotropic Structure

Figure 2 displays the isotropic part of 3D2015_07Sv at different depths in the mantle. The long wavelength component of 3D2015_07Sv shear waves heterogeneities is consistent with DR2012, our previous seismic model [Debayle and Ricard, 2012]. Like in other recent seismic models (Figure S4), we find a very strong

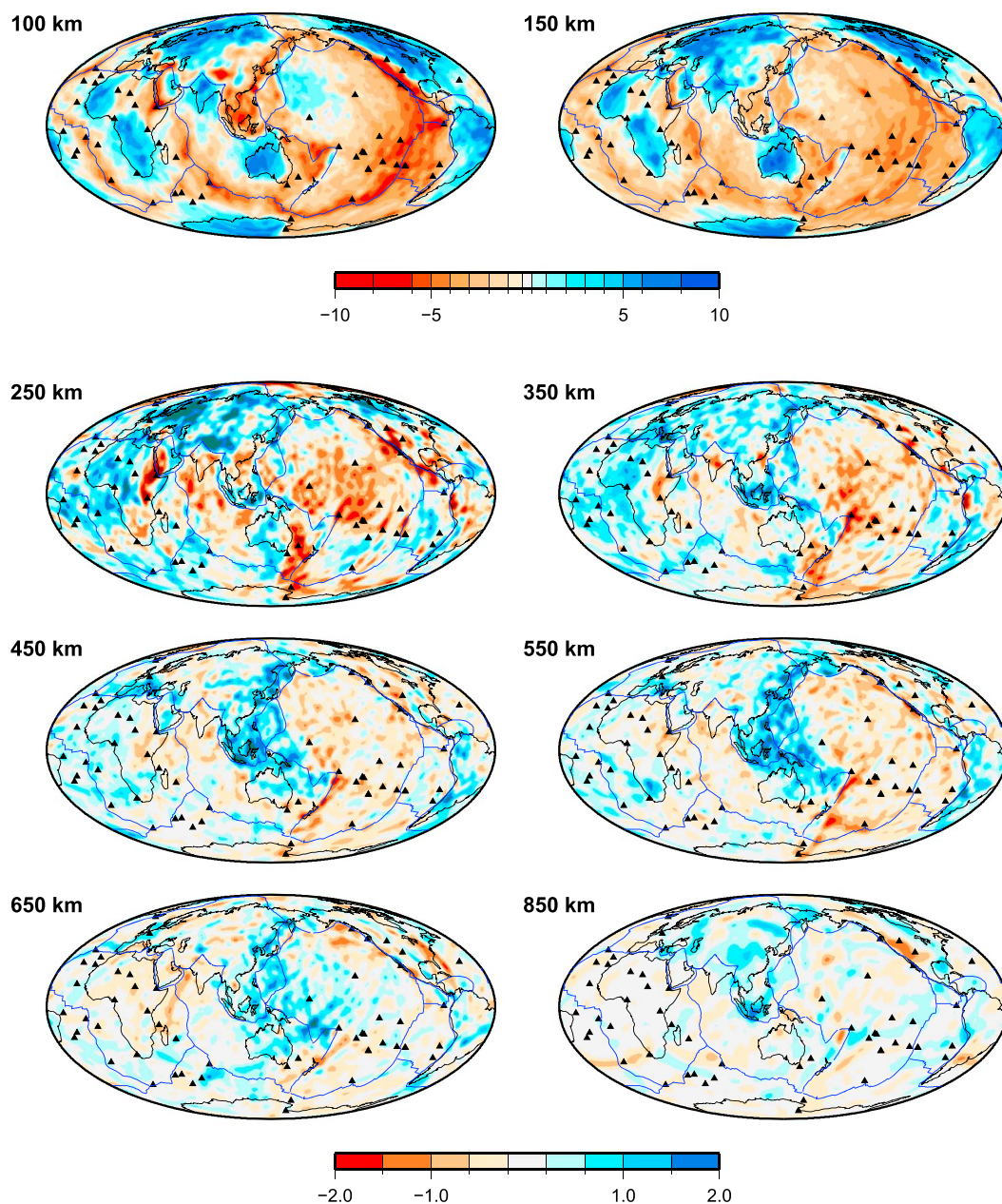


Figure 2. SV velocity distribution at different depths in 3D2015_07Sv. Perturbations from the reference velocity in percent are displayed by color coding. The velocity varies from -10% to $+10\%$ from the average value in the uppermost 200 km. At greater depths, shear velocity perturbations are between -2% and $+2\%$ to emphasize smaller contrasts.

correlation with surface tectonics in the uppermost 200 km. Oceanic ridges have a strong slow velocity signature down to 100 km depth. This signature is rather shallow and vanishes between 100 and 150 km depths. Archean and Proterozoic cratons display high velocities down to 200–250 km depth, depending on the location. Phanerozoic lithosphere is generally thinner than 100 km, except beneath the Andes where active subduction is present, and beneath Tibet, where continental collision of Asia and southern Eurasia favors underthrusting by a high-velocity Indian mantle [Priestley *et al.*, 2006].

Below 200 km depth the correlation with surface tectonics vanishes (Figure 2), and the strength of seismic heterogeneities decreases from $\pm 6\%$ at 200 km depth to $\pm 2\%$ in the transition zone. In the transition zone, the strongest contrasts are larger than 1% and are associated with broad fast velocity regions beneath ponding slabs, around the Pacific ocean.

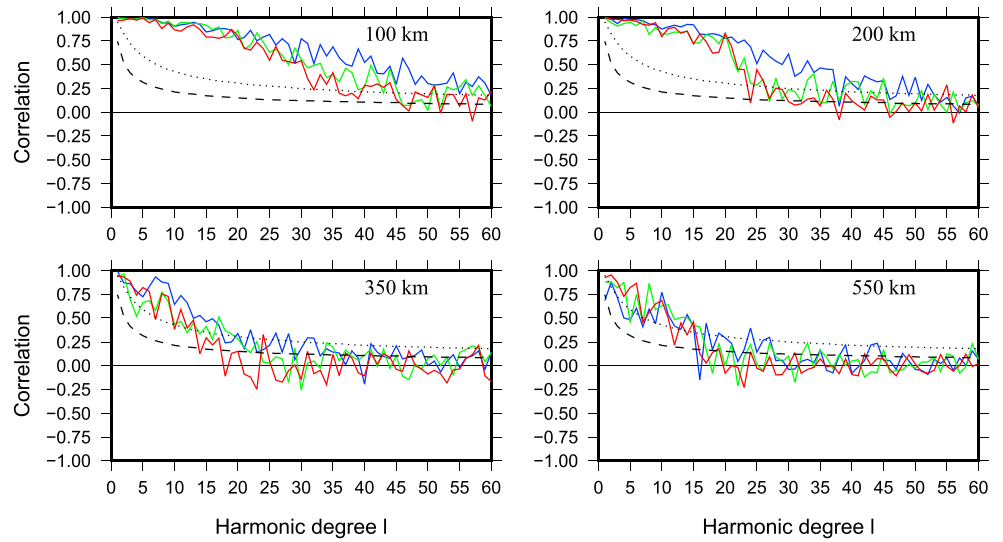


Figure 3. Correlations as a function of degree between 3D2015_07Sv and SL2013sv [Schaeffer and Lebedev, 2013] (blue line); 3D2015_07Sv and SEMum2 [French et al., 2013] (red line); SEMum2 [French et al., 2013] and SL2013sv [Schaeffer and Lebedev, 2013] (green line). Correlations are computed at 150 km, 250 km, 350km, and 550 km. On each figure the dotted and dashed lines indicate respectively the 95% and 66% significance levels.

Finally, in 3D2015_07Sv, the use of long-period surface waves and their higher modes allows us to extract additional information on shear wave velocities down to about 1000 km depth [Durand et al., 2015], while we were limited to the upper mantle only in DR2012.

5. Comparison With Other Models

We compare 3D2015_07Sv with two recent seismic models of the upper mantle, SL2013sv [Schaeffer and Lebedev, 2013], and SEMum2 [French et al., 2013]. Shear velocity maps at different depths in 3D2015_07Sv, SL2013sv, and SEMum2 are displayed in Figure S4. Figure 3 displays the correlation at the same depths between all models. The correlation between two seismic models A and B at a given depth z is as follows:

$$C(l, z) = \frac{\sum_{m=-l}^l A_l^m(z) B_l^{m*}(z)}{S_A(l, z) S_B(l, z)} \tag{1}$$

where A_l^m are the spherical harmonic coefficients at degree l and azimuthal order m of model A, $*$ denotes the complex conjugate, and S_A is the amplitude spectrum of model A. The spectra $S_A^2(l) = \sum_{m=-l}^l A_l^m A_l^{m*}$ of the three models are displayed in Figure S5. We also show in Figure S6 global correlations as a function of depth for spherical harmonic expansion of the models up to degrees 12, 35, and 60.

At 100 km depth, the best correlation is found between 3D2015_07Sv and SL2013sv. The correlation between these two models is above the 95% confidence level (i.e., there is 95% of chance that this correlation is not due to chance) up to degree 60, corresponding to wavelengths greater than about $l \sim (2\pi R)/60 \approx 667$ km. This value is very close to the nominal resolution of both models (~ 600 km). This suggests that the use of massive data sets with large redundancies allows averaging errors and building models consistent up to their nominal resolution. SEMum2 correlates at the 95% confidence level up to degrees 35 and 45 with 3D2015_07Sv and SL2013sv respectively.

At 200 km depths 3D2015_07Sv and SL2013sv are correlated with 95% confidence at all degrees (except for degree 37) up to degree 45. SEMum2 correlates with the two other models above the 95% confidence level up to degrees 23–27.

One explanation of the better agreement between 3D2015_07Sv and SL2013sv could be that they are built using similar approximations and are thus biased in the same way. This however is not likely, because these

models rely on different choices concerning the strategy used to extract information from the data, the period range of analysis, and the number of modes involved. 3D2015_07Sv results from the inversion of secondary observables, built up from the seismograms to reduce the nonlinearity of the waveform inversion. Fundamental mode and up to the fifth overtone Rayleigh waveforms are analyzed in the period range 40–400 s. SL2013sv involves a direct match of waveforms up to shorter periods (10–400 s) and using a larger number of overtone (>10). Although similar approximations are used, it is not likely that they affect in the same way waveforms analyzed at different periods and using a different number of overtones.

Another interpretation is that these two models involve massive data sets, so that data redundancy is sufficiently large to average most errors. Considering that the number of waveforms used in 3D2015_07Sv and SL2013sv is 1 order of magnitude greater than the one used in SEMum2, we believe that this is the most likely explanation. A resolution of about ~ 600 km is at the lower limit of what can be achieved with ray theory [Yoshizawa and Kennett, 2002]. This suggests that 3D2015_07Sv or SL2013sv can be used as starting models for further inversions using more sophisticated theory with the hope of extracting a coherent information on shorter wavelengths shear heterogeneities.

At 350 km depth, 3D2015_07Sv and SL2013sv still correlate at a slightly better level than other models up to degree 20. However, differences reduce and all correlation curves are above the 95% confidence level up to degrees 13–18 (Figure 3). Within the transition zone, all models are consistent close to the 95% confidence level up to degree 15 (corresponding to wavelengths ≥ 2600 km). In this depth interval, the coverage is limited by the distribution of subduction zone events (deep events which excite overtones, and/or large events which excite the fundamental mode at periods greater than 200 s). It is likely that because of a more limited coverage, redundancy is less efficient to average errors, so that differences between models are more influenced by modeling choices. These modeling choices include the period range of analysis, the number of overtones considered, the theory, the parameterization, and the regularization.

A significant difference is observed at 350 and 550 km depth between SL2013sv and the other two models (Figure S4). In 3D2015_07Sv and SEMum2, the dominant pattern at 550 km is a broad high velocity anomaly in a region spanning the eastern margin of Asia, the Philippine sea, Indonesia, Papua New Guinea, New Hebrides, and Fiji. Although subductions in these regions are well underlain at 350 km depth in SL2013sv, this broad velocity anomaly is weaker at 550 km depth, and the strongest signal is associated with a band of high velocities stretching westward from the eastern margin of Asia to Tibet and Anatolia. Schaeffer and Lebedev [2013] associate this signal with remnants of subduction after the closure of the Tethys ocean. It is likely that this signal is picked up by higher modes in the period ranges 10–40 s, as it is not observed in the other two models which consider Rayleigh waveforms at periods greater than 40 s. This suggests that in the transition zone, modeling choices remain the most important cause of the observed differences between seismic models.

Finally, an important point is that the agreement between these recent seismic models has significantly improved compared to what was achieved with models built only a few years ago. Debayle and Ricard [2012] and Meschede and Romanowicz [2015] found an agreement up to degrees 20–30 for most seismic models in the uppermost 200 km, while the agreement was confined to harmonic degree ≤ 10 in the transition zone.

6. Azimuthal Anisotropy

Maps displaying azimuthal anisotropy at different depths in the mantle can be found in Figure S7. We also show in Figure S8 the azimuthal anisotropy computed in 3D2015_07Sv as a function of plate velocity. Figure S8 confirms, with a data set expanded by a factor 3.5, Debayle and Ricard [2013]'s result that only plates moving faster than about 4 cm yr^{-1} produce sufficient shear at their base to organize the asthenospheric anisotropy at the scale of the entire tectonic plates.

In Figure 4a we compare the average amplitude of azimuthal anisotropy as a function of depth, calculated for oceanic and continental regions. Significant azimuthal anisotropy ($\geq 1\%$) is found in the uppermost 200 km of the mantle. A striking result is that azimuthal anisotropy does not extend deeper beneath continents than beneath oceans. In oceanic regions, azimuthal anisotropy peaks at 125 km depth, in agreement with previous studies suggesting an intense deformation in the oceanic asthenosphere [e.g., Nishimura and Forsyth, 1989; Debayle and Ricard, 2013]. Beneath continents, anisotropy decreases from 2.25% at 50 km depth to about 1% at 200 km. In Figure 4b, we use the plate velocity value of 4 cm yr^{-1} , which is found to represent a threshold for the large-scale organization of azimuthal anisotropy (Figure S8), to split continents and ocean in fast and

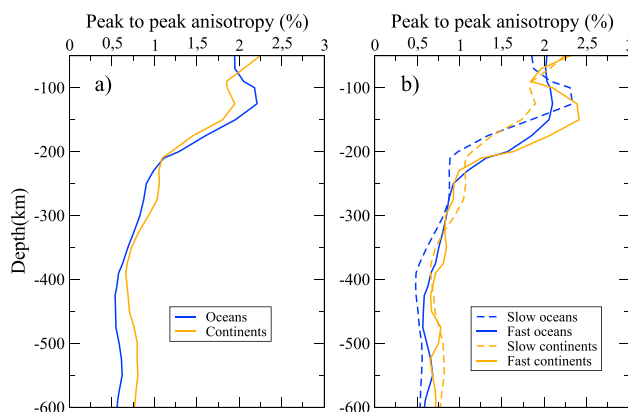


Figure 4. The azimuthal anisotropy in 3D2015_07Sv is plotted as a function of depth. Figure 4a shows that there is no clear difference in the depth extent of azimuthal anisotropy beneath continents and oceans. In Figure 4b, we split oceans and continents in fast and slow parts, based on Figure S8. Fast/slow continents or oceans are those for which the plate velocities are greater/smaller than 4 cm yr^{-1} . Although anisotropy extend slightly deeper beneath fast plates, there is no clear ocean/continent difference.

depths of 80–250 km. We observe a weak azimuthal anisotropy in the depth range 250–400 km beneath continents, where they find significant radial anisotropy. A simple explanation is to invoke olivine crystals that would be preferentially aligned in the horizontal plane (this would produce radial anisotropy with Sh waves traveling faster than Sv waves) but with no coherent azimuthal organization on a large scale. An exception could be the fastest continent on Earth, Australia, for which azimuthal anisotropy is significant and oriented north-south, parallel to the present-day Absolute Plate Motion (APM) down to at least 350 km depth (Figure S7), consistent with the depth extent found for radial anisotropy.

7. Conclusion

This paper presents 3D2015_07Sv, a new Sv wave model of the upper mantle and transition zone. 3D2015_07Sv is based on 1,359,470 vertical component Rayleigh waves recorded between 1976 and July 2015, and forms the basis of an evolutionary model, that will be updated on a regular basis, following the publication of the monthly CMT catalog. The model and its updates will be made freely available to the community.

Synthetic tests show that 3D2015_07Sv has an horizontal “nominal” resolution of $\sim 600 \text{ km}$. Comparison of 3D2015_07Sv with two other recent seismic models suggests that in the uppermost 200 km, the use of massive data sets with large redundancies is the most important factor in reducing differences between models. In this depth interval, data redundancy allows averaging errors, so that it is now possible to build global upper mantle models that are consistent up to their nominal resolution (degree 60, corresponding to wavelengths of $\sim 650 \text{ km}$), a significant progress compared to a few years ago. In the transition zone, the number of available data reduces, and modeling choices remain the most important cause of the observed differences between seismic models. The most recent seismic models agree up to degree 15, which represents an improvement compared to the previous generation of models, but remains far from the nominal resolution.

3D2015_07Sv contains significant azimuthal anisotropy in the uppermost 200 km of the mantle, and this anisotropy does not extend deeper under continents than under oceans. This contrasts with previous results suggesting that radial anisotropy extend deeper beneath continents than under oceans [Gung *et al.*, 2003]. A possible explanation is that the alignment of olivine crystal is preferentially horizontal in the depth range 250–400 km beneath most continents and azimuthally random at large scale. As most continents, except India and Australia, are located on plates moving slower than $\sim 4 \text{ cm yr}^{-1}$, this is consistent with the idea that azimuthal anisotropy aligns on a large scale with the present plate motion only for plate velocities larger than $\sim 4 \text{ cm yr}^{-1}$.

slow parts. We find that azimuthal anisotropy extends about 50 km deeper beneath fast-moving plates. However, we still find no ocean/continent difference in the depth extent of azimuthal anisotropy under fast- and slow-moving plates. We checked that the decrease of azimuthal anisotropy is not due to a decrease of resolution. In Figure S9, we show using Voronoi diagrams that the azimuthal coverage allows us to retrieve azimuthal anisotropy everywhere in the upper mantle.

Our azimuthal anisotropy results contrast from the finding by Gung *et al.* [2003], that radial anisotropy with Sh waves traveling faster than Sv waves is present beneath continents in the depth range 250–400 km, deeper than under oceans where it is found at

Acknowledgments

This work was supported by the French ANR SEISGLOB ANR-11-BLANC-SIMI5-6-016-01. We thank Thomas Bodin for suggestions that helped to improve an earlier version of the manuscript, the Associate Editor, Andreas Fichtner, and an anonymous reviewer for constructive reviews. We thank the IRIS and RESIF data centers. We used data from several temporary experiments including various PASSCAL deployments in the world and the SKIPPY and KIMBA experiments in Australia. Other data from French temporary experiments in Afar, French Polynesia, Egean-Anatolia region (SIMBAAD temporary experiment), and Tibet were provided by the RESIF data distribution system. Our tomographic model, 3D2015_07Sv, and its updates are available via Eric Debayle's webpage.

References

- Backus, G., and F. Gilbert (1968), The resolving power of gross Earth data, *Geophys. J. R. Astron. Soc.*, *16*, 169–205.
- Barruol, G., D. Bosch, V. Clouard, E. Debayle, M. Doin, M. Godard, F. Fontaine, F. Masson, A. Tommasi, and C. Thoraval (2002), Polynesian lithosphere and upper mantle experiment (PLUME): The south Pacific superswell under investigation, *Eos Trans. AGU*, *83*(45), 510–514.
- Beucler, E., E. Stutzmann, and J. Montagner (2003), Surface wave higher-mode phase velocity measurements using a roller-coaster-type algorithm, *Geophys. J. Int.*, *155*(1), 289–307.
- Chen, M., F. Niu, Q. Liu, J. Tromp, and X. Zheng (2015), Multiparameter adjoint tomography of the crust and upper mantle beneath East Asia: 1. Model construction and comparisons, *J. Geophys. Res. Solid Earth*, *120*, 1762–1786, doi:10.1002/2014JB011638.
- Debayle, E. (1999), SV-wave azimuthal anisotropy in the Australian upper mantle: Preliminary results from automated Rayleigh waveform inversion, *Geophys. J. Int.*, *137*(3), 747–754.
- Debayle, E., and Y. Ricard (2012), A global shear velocity model of the upper mantle from fundamental and higher Rayleigh mode measurements, *J. Geophys. Res.*, *117*, B10308, doi:10.1029/2012JB009288.
- Debayle, E., and Y. Ricard (2013), Seismic observations of large-scale deformation at the bottom of fast-moving plates, *Earth Planet. Sci. Lett.*, *376*, 165–177, doi:10.1016/j.epsl.2013.06.025.
- Debayle, E., and M. Sambridge (2004), Inversion of massive surface wave data sets: Model construction and resolution assessment, *J. Geophys. Res.*, *109*, B02316, doi:10.1029/2003JB002652.
- Durand, S., E. Debayle, and Y. Ricard (2015), Rayleigh wave phase velocity and error maps up to the fifth overtone, *Geophys. Res. Lett.*, *42*, 3266–3272, doi:10.1002/2015GL063700.
- Dziwonski, A., T. Chou, and J. Woodhouse (1981), Determination of earthquake source parameters from waveform data for studies of global and regional seismicity, *J. Geophys. Res.*, *86*(B4), 2825–2852, doi:10.1029/JB086iB04p02825.
- Fichtner, A., and T. van Leeuwen (2015), Resolution analysis by random probing, *J. Geophys. Res. Solid Earth*, *120*, 5549–5573, doi:10.1002/2015JB012106.
- Fichtner, A., B. L. N. Kennett, H. Igel, and H.-P. Bunge (2009), Full seismic waveform tomography for upper-mantle structure in the Australasian region using adjoint methods, *Geophys. J. Int.*, *179*(3), 1703–1725, doi:10.1111/j.1365-246X.2009.04368.x.
- Fichtner, A., B. L. N. Kennett, H. Igel, and H.-P. Bunge (2010), Full waveform tomography for radially anisotropic structure: New insights into present and past states of the Australasian upper mantle, *Earth Planet. Sci. Lett.*, *290*(3–4), 270–280, doi:10.1016/j.epsl.2009.12.003.
- French, S., V. Lekic, and B. Romanowicz (2013), Waveform tomography reveals channeled flow at the base of the oceanic asthenosphere, *Science*, *342*(6155), 227–230, doi:10.1126/science.1241514.
- Gung, Y., M. Panning, and B. Romanowicz (2003), Global anisotropy and the thickness of continents, *Nature*, *422*(6933), 707–711, doi:10.1038/nature01559.
- Komatitsch, D., J. Ritsema, and J. Tromp (2002), The spectral-element method, beowulf computing, and three-dimensional seismology, *Science*, *298*, 1737–1742.
- Lebedev, S., and R. D. van der Hilst (2008), Global upper-mantle tomography with the automated multimode inversion of surface and S-wave forms, *Geophys. J. Int.*, *173*(2), 505–518, doi:10.1111/j.1365-246X.2008.03721.x.
- Li, X., and B. Romanowicz (1995), Comparison of global waveform inversions with and without considering cross-branch modal coupling, *Geophys. J. Int.*, *121*(3), 695–709, doi:10.1111/j.1365-246X.1995.tb06432.x.
- Marquering, H., R. Snieder, and G. Nolet (1996), Waveform inversion and the significance of surface-wave mode coupling, *Geophys. J. Int.*, *124*, 258–278.
- Meschede, M., and B. Romanowicz (2015), Lateral heterogeneity scales in regional and global upper mantle shear velocity models, *Geophys. J. Int.*, *200*(2), 1076–1093, doi:10.1093/gji/ggu424.
- Montagner, J.-P., B. Marty, E. Stutzmann, D. Sicilia, M. Cara, R. Pik, J.-J. L  v  que, G. Roullet, E. Beucler, and E. Debayle (2007), Mantle upwellings and convective instabilities revealed by seismic tomography and helium isotope geochemistry beneath eastern Africa, *Geophys. Res. Lett.*, *34*, L21303, doi:10.1029/2007GL031098.
- Nataf, H., and Y. Ricard (1995), 3SMAC: An a priori tomographic model of the upper mantle based on geophysical modeling, *Phys. Earth Planet. Inter.*, *95*, 101–122.
- Nishimura, C., and D. Forsyth (1989), The anisotropic structure of the upper mantle in the Pacific, *Geophys. J. Int.*, *96*(2), 203–229, doi:10.1111/j.1365-246X.1989.tb04446.x.
- Priestley, K., E. Debayle, D. McKenzie, and S. Pilidou (2006), Upper mantle structure of eastern Asia from multimode surface waveform tomography, *J. Geophys. Res.*, *111*, B10304, doi:10.1029/2005JB004082.
- Salauen, G., H. A. Pedersen, A. Paul, V. Farra, H. Karabulut, D. Hatzfeld, C. Papazachos, D. M. Childs, C. Pequegnat, and S. Team (2012), High-resolution surface wave tomography beneath the Aegean-Anatolia region: Constraints on upper-mantle structure, *Geophys. J. Int.*, *190*(1), 406–420, doi:10.1111/j.1365-246X.2012.05483.x.
- Schaeffer, A. J., and S. Lebedev (2013), Global shear speed structure of the upper mantle and transition zone, *Geophys. J. Int.*, *194*(1), 417–449, doi:10.1093/gji/ggt095.
- Spetzler, J., and R. Snieder (2001), The effect of small-scale heterogeneity on the arrival time of waves, *Geophys. J. Int.*, *145*, 786–796.
- Trampert, J., and J. Woodhouse (1995), Global phase velocity maps of Love and Rayleigh waves between 40 and 150 seconds, *Geophys. J. Int.*, *122*, 675–690.
- Tromp, J., C. Tape, and Q. Liu (2005), Seismic tomography, adjoint methods, time reversal and banana-doughnut kernels, *Geophys. J. Int.*, *160*(1), 195–216, doi:10.1111/j.1365-246X.2004.02453.x.
- van Heijst, H., and J. Woodhouse (1997), Measuring surface-wave overtone phase velocities using a mode branch stripping technique, *Geophys. J. Int.*, *131*, 209–230.
- Yoshizawa, K., and G. Ekstrom (2010), Automated multimode phase speed measurements for high-resolution regional-scale tomography: Application to North America, *Geophys. J. Int.*, *183*(3), 1538–1558, doi:10.1111/j.1365-246X.2010.04814.x.
- Yoshizawa, K., and B. Kennett (2002), Determination of the influence zone for surface wave paths, *Geophys. J. Int.*, *149*, 441–454.
- Zhou, Y., F. Dahlen, and G. Nolet (2004), Three-dimensional sensitivity kernels for surface wave observables, *Geophys. J. Int.*, *158*(1), 142–168, doi:10.1111/j.1365-246X.2004.02324.x.
- Zhu, H., and J. Tromp (2013), Mapping tectonic deformation in the crust and upper mantle beneath Europe and the North Atlantic Ocean, *Science*, *341*(6148), 871–875, doi:10.1126/science.1241335.
- Zhu, H., E. Bozdag, D. Peter, and J. Tromp (2012), Structure of the European upper mantle revealed by adjoint tomography, *Nat. Geosci.*, *5*(7), 493–498, doi:10.1038/ngeo1501.